



RESEARCH PAPER

Acta Mech. Sin., Vol.39, 723007 (2023) https://doi.org/10.1007/s10409-023-23007-x

Dynamic phononic crystals with spatially and temporally modulated circuit networks

Qian Wu^{1†}, Honghua Qian^{1†}, Yangyang Chen^{2*}, and Guoliang Huang^{1*}

¹Department of Mechanical and Aerospace Engineering, University of Missouri, Columbia, Missouri 65211, USA; ²Department of Mechanical and Aerospace Engineering, The Hong Kong University of Science and Technology, Clear Water Bay, Hong Kong 999077, China

Received January 7, 2023; accepted February 13, 2023; published online May 17, 2023

Elastic wave mitigation covering multiple broad bands is highly demanded for modern applications in wave control. Here, we report both theoretically and experimentally on the complete investigation of a series of dynamic phononic crystal beams integrated with circuit networks decorated with both spatial and temporal modulation. They are capable of practicing multi-band flexural wave mitigation with convenient tunability and broadband operability. The electromechanical interaction through piezoelectric shunts allows for energy exchange between electrical and mechanical modes and gives rise to Bragg forbidden bands. The key contribution of this work lies in the inclusion of spatial and temporal modulation that is applied solely in circuit networks and improves wave mitigation abilities in terms of operable frequency range. Specifically, the spatial modulation of circuit network effectively broadens the wave attenuation band by creating space-Bragg forbidden bands for electrical modes and thus extending the electromechanical coupling range. The temporal modulation, on the other hand, generates time-Bragg band gaps by linearly translating the fundamental electromechanical mode in terms of frequency. More importantly, both seemingly complicated approaches are simply based on the convenient tuning of a single resistor in the circuit network. This advantage later facilitates the experimental evidences of the transmission characteristics of the spatially and temporally modulated configurations. We believe the dynamic phononic crystals are highly promising for the next-generation applications such as tunable multi-band filters.

Electromechanical coupling, Circuit network, Flexural waves, Spatial modulation, Temporal modulation

Citation: Q. Wu, H. Qian, Y. Chen, and G. Huang, Dynamic phononic crystals with spatially and temporally modulated circuit networks, Acta Mech. Sin. 39, 723007 (2023), https://doi.org/10.1007/s10409-023-23007-x

1. Introduction

Manipulation of elastic waves with periodically structured lattices has been attracting increased attention for its potential applications in mechanical wave mitigations and vibration attenuations [1-3]. The central point is to generate forbidden bands covering the frequencies of interest [4]. There exist two general approaches to realizing forbidden bands: mechanical metamaterials and phononic crystals (PhCs). Both of them rely on carefully tailored periodic structures

Executive Editor: Gengkai Hu

but differ fundamentally in the working mechanism. Mechanical metamaterials operate on the basis of local resonances of subwavelength units and thus delivers only narrowband wave mitigation at their resonances [5-9]. PhCs, on the other hand, features periodic structural inclusions whose geometrical scale is comparable to operating wavelengths [10-14]. They allow in general for much broader forbidden bands than metamaterials and appear to be more favorable for practical applications. Thus far, most of the existing efforts on mechanical PhCs have been focused on designing passive structures for manipulating elastic waves. This inevitably hinders the broadband operability and reconfigurability.

To address the above fundamental limitation, standalone

[†] These authors contributed equally to this work.

^{*}Corresponding authors. E-mail addresses: maeychen@ust.hk (Yangyang Chen); huangg@missouri.edu (Guoliang Huang)

piezoelectric (PZT) shunts have been extensively adopted as an efficient way to actively manipulate elastic wave propagation [3, 15-20]. Thanks to the convenient tuning of the mechanical properties of PZT materials by controlling the impedance of shunting circuits, exotic wave phenomena and applications have been proposed, such as programmable metasurfaces [21-23], asymmetric wave propagation [24-26] and so forth. Recently, researchers proposed that connecting circuit network to PZT-based PhCs can greatly benefit to broadband wave mitigation and vibration suppression [27-29]. The key point is that the interactions between the electrical and mechanical degrees of freedom in this hybrid phononic crystal (HPhC) result in broad Bragg band gaps. Theoretically, a multi-degree-of-freedom electric network could provide a new avenue to create electromechanical energy exchange and therefore attenuate vibrations in additional frequency ranges. The recent efforts on HPhCs reveal that the interactions of electrical and mechanical modes correspond to mode veering or locking depending on the group velocities of the coupled modes [29, 30]. Bergamini et al. [29] also experimentally validated the broadband wave mitigation behavior of HPhCs with alternating inductors . A digitally programmable HPhC was then realized with tunable mechanical properties by integration of electrical and mechanical parts [31]. Two distinct external circuit networks connected to a PZT-based beam, the LC-based high-pass and band-pass networks, were suggested [32]. In addition to flexural waves, Flores Parra et al. [33] proposed a HPhC for controlling longitudinal waves. The realization of interactions between longitudinal and electrical modes is through multiple pairs of PZT patches, which enables tunability. Very recently, adaptive and tunable nonreciprocal propagation of elastic wave in HPhCs is proposed by Zheng et al. [34] via a nonreciprocal circuit network. The resulting forbidden band is attached with distinct attenuation characteristics in opposite propagation directions.

In this work, we first revisit and enrich the elastodynamic behavior of HPhCs by deepening the understanding of the multi-physical mechanism and then investigate a new dynamic phononic crystal with spatial and temporal modulation in circuit networks [35-38]. Notably, the introduction of modulation can dramatically improve the wave mitigation performance in terms of the bandwidth and number of forbidden bands. The paper is organized primarily into two sections. In the first section, we establish a comprehensive theoretical model with the transfer matrix method and a discrete representation to theoretically characterize the wave dynamics of a HPhC with a monatomic circuit network. Its transmission characteristics are then examined by the comparison of numerical simulations and experimental demonstration. In the second section, we propose a new dynamic phononic

crystals (DPhC) with spatially and temporally modulated circuit networks to showcase the unprecedented wave mitigation. Dispersion analyses are conducted to reveal additional interactions of mechanical and electrical modes for creating new band-gaps at different frequency ranges. Numerical simulations and experimental testings are then carried out to confirm the predicted wave dynamics.

2. Hybrid phononic crystals with uniform circuit network

The physical construction of the mechanical parts of HPhCs with a uniform circuit network and the DPhCs with modulated circuit networks is shown in Fig. 1a. A periodic array of PZT patches are bonded on an aluminum host beam. These PZT patches are shunted with external electrical nodes. The nodes are then interconnected through inductors and hence constitute a circuit network. The HPhC decorated with uniform circuit network is first schematically depicted in Fig. 1b, with Fig. 1c showing the physical circuit components to enable the tunable synthetic inductor by a digital potentiometer [31]. There are two degrees of freedom in the onedimensional HPhC with w being the flexural displacement and V the voltage of node. While w corresponds to the flexural mode, V corresponds to the electrical mode propagating in the circuit network, a second-order transmission line. The two modes are coupled through the electromechanical coupling of the PZT materials. Throughout the paper, the collective behaviors of two coupled modes are investigated based on unit cell analyses with periodicity, as shown in Fig. 1d.

2.1 Dynamic transfer matrix method

First, we start with analytically deriving the dispersion relation of the HPhC with a uniform inductor-based network using transfer matrix method (TMM) [34]. The HPhC can be divided into two sections. While section A of the beam includes a shunted PZT patch, section B is purely an aluminum host beam ($\rho_s = 2700 \text{ kg/m}^3$, $E_s = 76 \text{ GPa}$). The three-dimensional problem can be simplified into a two-dimensional one using plane-stress assumptions. Since the upper surface of PZT element is free, the traction on it is assumed to be zero. The relationship of the electrical and mechanical responses in the PZT material can be described as [39]

$$S_1 = S_{11}^{E} T_1 + d_{31} E_3,$$

$$D_3 = \epsilon_{33}^{T} E_3 + d_{31} T_1,$$
(1)

where T_1 and E_3 are the horizontal stress and the electrical field in the thickness direction of the PZT element. S_{11}^{E}

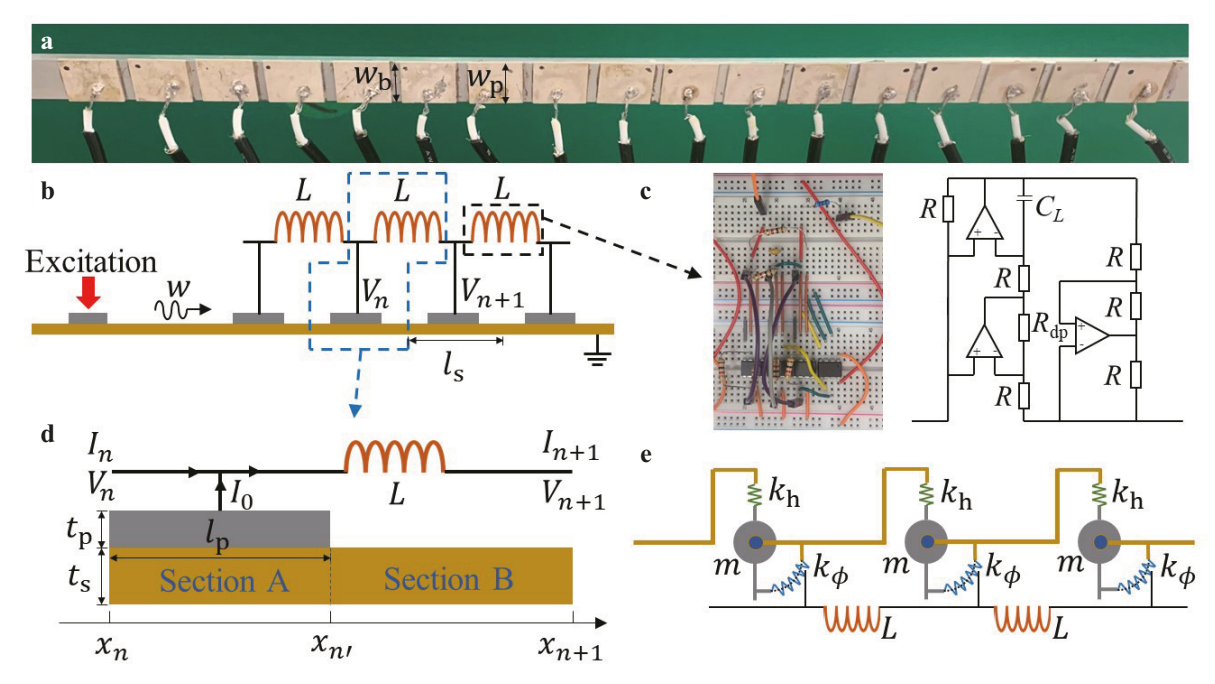


Figure 1 a Photo of the mechanical part of the PZT-based HPhCs and DPhCs. **b** Schematic of the HPhC with a uniform circuit network. **c** Circuit-enabled tunable synthetic inductor, where $R_{\rm dp}$ is a digital potentiometer controlled by an external micro-controller (Arduino Mega 2560), The effective inductance is determined as $L = R^3 C_L / R_{\rm dp}$, where all resistors are the same and valued as R. **d** Schematic of the unit cell. The host beam is made of aluminum. The PZT patches are PZT-5A. **e** Discrete representation of the HPhC.

 $-1.64 \times 10^{-11} \, \mathrm{Pa^{-1}}$, $\epsilon_{33}^{\mathrm{T}} = 1900$ and $d_{31} = -1.71 \times 10^{-10} \, \mathrm{C/N}$ represent compliance coefficient at constant electric field, dielectric coefficient at constant stress and electromechanical coupling coefficient, respectively. Since the considered beam is thin with respect to operating wavelengths, we follow the Euler-Bernoulli beam theory and assume the harmonic solutions $w = w_0 \mathrm{e}^{\mathrm{j}(kx-\omega t)}$ and $V = V_0 \mathrm{e}^{\mathrm{j}(kx-\omega t)}$ for mechanical and electrical modes, respectively. This way, we define a state variable vector $\mathbf{Y} = (w, w_{,x}, M, Q)^{\mathrm{T}}$, representing the displacement, bending curvature, moment and shear force. They are related according to

$$\begin{split} \frac{\partial w}{\partial x} &= w_{,x}, \\ D_{A} \frac{\partial w_{,x}}{\partial x} &= M + \alpha V, \\ \frac{\partial M}{\partial x} &= -Q, \\ \frac{\partial Q}{\partial x} &= -\omega^{2} \rho_{A} w, \end{split} \tag{2}$$

where $\alpha = d_{31}w_pz_p/S_{11}^E$ denotes the mode coupling coefficient between electrical and mechanical modes [34], and the effective mass density and bending stiffness can be expressed, respectively, as $\rho_A = \rho_s w_b t_s + \rho_p w_p t_p$ and $D_A = E_s \left(\frac{w_b t_s^3}{12} + w_b t_s z_s^2 \right) + E_p \left(\frac{w_p t_p^3}{12} + w_p t_p z_p^2 \right)$. Here, ρ_p and E_p are the mass density and Young's modulus (the inverse of S_{11}^E) of the PZT material, respectively. z_s and z_p are the distances of the host beam and the PZT patch from their respective cen-

tral axes to the neutral axis of section A whose location can be calculated by

$$z_0 = \frac{E_p t_p (t_p / 2 + t_s) + E_s t_s^2 / 2}{E_p t_p + E_s t_s}.$$
 (3)

When the PZT patch is deformed, the charge generated on its top surface results in a current flowing into the circuit network, i.e.,

$$I_0 = -\mathrm{i}\omega\alpha \mathbf{J}_{\mathrm{A}}(\mathbf{Y}_{n'} - \mathbf{Y}_n). \tag{4}$$

Similarly, the mechanical part of section B can be characterized by

$$\frac{\partial w}{\partial x} = w_{,x},
D_{\rm B} \frac{\partial w_{,x}}{\partial x} = M,
\frac{\partial M}{\partial x} = -Q,
\frac{\partial Q}{\partial x} = -\omega^2 \rho_{\rm B} w,$$
(5)

with $\rho_B = \rho_s w_b t_s$ and $D_B = E_s w_b t_s^3 / 12$. Based on Eq. (2), the transfer matrix form for section A can be written as

$$\mathbf{A}_{\mathbf{A}} \frac{\partial \mathbf{Y}}{\partial x} = \mathbf{B}_{\mathbf{A}} \mathbf{Y} + \mathbf{J}_{\mathbf{A}} V, \tag{6}$$

where $\mathbf{A}_{A} = \text{diag}(1, D_{A}, 1, 1), \mathbf{J}_{A} = (0, \alpha, 0, 0)^{T}$ and

$$\mathbf{B}_{\mathbf{A}} = \begin{bmatrix} 0 & 1 & 0 & 0 \\ 0 & 0 & 1 & 0 \\ 0 & 0 & 0 & -1 \\ -\rho_{\mathbf{A}}\omega^2 & 0 & 0 & 0 \end{bmatrix}. \tag{7}$$

The solution can be written in an exponential form as follows:

$$\mathbf{Y}_{n'} = -\mathbf{C}_{\Delta}^{-1} \mathbf{J}_{A} V_{n} + \mathbf{F} \mathbf{C}_{\Delta}^{-1} \mathbf{J}_{A} V_{n} + \mathbf{F} \mathbf{Y}_{n}, \tag{8}$$

in which $C_A = A_A^{-1}B_A$ and $F = e^{C_A l_p}$. Similar derivation can be done for section B:

$$\mathbf{Y}_{n+1} = \mathbf{e}^{\mathbf{C}_{\mathbf{B}}(l_{\mathbf{s}} - l_{\mathbf{p}})} \mathbf{Y}_{n'} = \mathbf{H} \mathbf{Y}_{n'}, \tag{9}$$

in which $C_B = A_B^{-1}B_B$ with $A_B = \text{diag}(1, D_B, 1, 1)$ and

$$\mathbf{B}_{\mathrm{B}} = \begin{bmatrix} 0 & 1 & 0 & 0 \\ 0 & 0 & 1 & 0 \\ 0 & 0 & 0 & -1 \\ -\rho_{\mathrm{B}}\omega^{2} & 0 & 0 & 0 \end{bmatrix}. \tag{10}$$

The treatment on the electrical part is based on the Kirchhoff's circuit laws. The electrical mode can be described with periodicity by

$$I_{n+1} = I_0 + I_n, (11)$$

$$V_{n+1} = -ZI_{n+1} + V_n, (12)$$

where $Z = j\omega L$ is the impedance of the inductor in the circuit network between the nodes of two adjacent PZT patches. In particular, I_n represents the current from the PZT patch to the external circuit network and reads

$$I_n = -j\omega\alpha \mathbf{J}_{\mathbf{A}}(\mathbf{Y}_{n'} - \mathbf{Y}_n) - j\omega C_{\mathbf{p}} V_n, \tag{13}$$

with $C_p = \epsilon_{33}^T w_p l_p / t_p$. In consideration of the interaction of the mechanical and electrical parts, we define a global state variable vector $\mathbf{X} = [\mathbf{Y}, V, I]^T$. Combining Eqs. (8),(9),(11), and (12), the relationship of global state variables at positions x_n and x_{n+1} can be represented by

$$\mathbf{M}_{1}\mathbf{X}_{n} = \mathbf{M}_{r}\mathbf{X}_{n+1},\tag{14}$$

where

$$\mathbf{M}_{1} = \begin{bmatrix} \mathbf{I} & 0 & 0 \\ j\omega\alpha\mathbf{J}_{A}\mathbf{H}^{-1} & 0 & 1 \\ 0 & 1 & -Z \end{bmatrix}, \tag{15}$$

$$\mathbf{M}_{r} = \begin{bmatrix} \mathbf{H}\mathbf{F} & \mathbf{G} & 0 \\ j\omega\alpha\mathbf{J}_{B} & -j\omega l_{p} & 1 \\ 0 & 1 & 0 \end{bmatrix}. \tag{16}$$

with $G = \mathbf{HFC}_{A}^{-1}\mathbf{J}_{A} - \mathbf{HC}_{A}^{-1}\mathbf{J}_{A}$. As a result, we conveniently obtain the transfer matrix given by

$$\mathbf{T} = \mathbf{M}_{\mathbf{r}}^{-1} \mathbf{M}_{\mathbf{l}}.\tag{17}$$

According to the Bloch Floquet condition $e^{jkl_s}\mathbf{X}_n = \mathbf{X}_{n+1}$, we can plot the dispersion curves for the HPhC with a uniform circuit network by solving the following eigenvalue problem for the wave number k in terms of the angular frequency ω

$$[\mathbf{T}(\omega) - e^{jkl_s}\mathbf{I}]\mathbf{X}_n = 0. \tag{18}$$

2.2 Discrete model

In addition to the TMM based on the Euler-Bernoulli assumptions, one can discretize the system using a spring-mass representation [40, 41]; see Fig. 1e. The proposed model has three degrees of freedom: the height of the mass w_n , rotation angle ϕ_n , and voltage V_n at the nth unit cell. In particular, the mechanical lattice is modulated by a Hookean spring k_h and a torsional one k_ϕ . The coupling between the mechanical and electrical chains is achieved through the electromechanical coupling of the torsional spring. In this case, the constitutive relation reads

$$T_{n} = k_{h}(w_{n-1} - w_{n} + l_{s}\phi_{n-1}),$$

$$M_{n} = k_{\phi}(\phi_{n-1} - \phi_{n}) + k_{e}V_{n},$$

$$Q_{n} = C_{p}V_{n} - k_{e}(\phi_{n-1} - \phi_{n}),$$
(19)

where M_n , Q_n and $k_e \propto \alpha$ denote the bending moment, charge and effective electromechanical coefficient for the discrete model, respectively. Summing the shear forces in the vertical direction yields a dynamical equation for w_n :

$$m_{e}\ddot{w}_{n} = T_{n} - T_{n+1}$$

$$= k_{h}(w_{n+1} + w_{n-1} - 2w_{n}) - l_{s}k_{h}(\phi_{n} - \phi_{n-1}), \tag{20}$$

where m_e is the effective on-site mass. On the other hand, summing the torques results in a dynamical equation for θ_n

$$I_{e}\ddot{\phi}_{n} = M_{n} - M_{n+1} - l_{s}T_{n+1}$$

$$= k_{\phi}(\phi_{n+1} + \phi_{n-1} - 2\phi_{n}) - k_{e}(V_{n+1} - V_{n})$$

$$+ l_{s}k_{h}(w_{n+1} - w_{n} - l_{s}\phi_{n}), \qquad (21)$$

where I_e is the effective moment of inertia. Last, according to the Kirchhoff's current law, we have

$$V_{n+1} + V_{n-1} - 2V_n - Lk_e(\ddot{\phi}_n - \ddot{\phi}_{n-1}) = LC_p \ddot{V}_n.$$
 (22)

Combining Eqs. (20)-(22), assuming harmonic solutions, and defining $\mathbf{U} = (w_n, \phi_n, V_n)^{\mathrm{T}}$ yields the following generalized eigenvalue problem:

$$\mathbf{D}\mathbf{U} = -\omega^2 \mathbf{M}\mathbf{U},\tag{23}$$

where the mass and dynamical matrices are, respectively, in forms of

$$\mathbf{M} = \begin{bmatrix} m_{e} & 0 & 0 \\ 0 & I_{e} & 0 \\ 0 & Lk_{e}(1 - e^{-jkl_{s}}) LC_{p} \end{bmatrix},$$
(24)

$$\mathbf{D} = \begin{bmatrix} 2k_{h}\epsilon(k) & l_{s}k_{h}(1 - e^{-jkl_{s}}) & 0\\ l_{s}k_{h}(e^{jkl_{s}} - 1) & 2k_{\phi}\epsilon(k) - l_{s}^{2}k_{h} & -k_{e}(e^{jkl_{s}} - 1)\\ 0 & 0 & 2\epsilon(k) \end{bmatrix},$$
(25)

with $\epsilon(k) = \cos k l_s - 1$. Similar to Eq. (18), solving for k in terms of ω gives the dispersion curves for the discrete spring-mass representation. Note that in the continuum limit, the discrete model can be reduced into a continuum govern by the Timoshenko beam theory:

$$\mu_{e} \frac{\partial^{2} w}{\partial x^{2}} - \mu_{e} \frac{\partial \phi}{\partial x} = \rho_{e} \ddot{w},$$

$$D_{e} \frac{\partial^{2} \phi}{\partial x^{2}} - k_{e} \frac{\partial \phi}{\partial x} + \mu_{e} (\frac{\partial w}{\partial x} - \phi) = I_{e} \ddot{\phi},$$

$$\frac{\partial^{2} V}{\partial x^{2}} - L_{e} k_{e} \frac{\partial \ddot{\phi}}{\partial x} = L_{e} C_{e} \ddot{V},$$
(26)

where the subscript "e" corresponds to an effective medium representation [40,41].

2.3 Dispersion curves of the hybrid phononic crystal

To validate the theoretical prediction, we conduct numerical simulations using COMSOL Multiphysics. Periodic boundary conditions with Floquet periodicity are designated on both ends of the unit cell (Fig. 1d). The lattice constant is $l_s = 12$ mm. The widths of the host beam and the PZT patches are selected to be $w_b = w_p = 10$ mm. Other geometrical parameters are given by $t_p = 0.5$ mm, $t_s = 2$ mm, $l_p = 10$ mm. All the resistors are identical with R = 1000 Ω and $C_L = 470$ nF. Note that throughout the paper, these geometrical and material properties are unchanged except for the tunable resistance R_{dp} that can tune L in space and time. The comparison between the analytical and numerical results is displayed in Fig. 2a. When the mode coupling is turned off, $\alpha = 0$, by disconnecting the external circuit network and the PZT-based beam, the electrical and mechanical modes are not coupled and hence independent. Their bands simply intersect with each other; see the pink scatterers and the inset in Fig. 2a. When the coupling is turned on, the weak perturbation caused by the coupling opens a small gap (mode veering) around the intersection at 7.5 kHz; see the black scatterers and the inset in Fig. 2a. Away from the coupling region, the curves remain nearly unaltered even in the presence of the coupling. In addition, the analytical results agree very well with the simulation, especially at low frequencies, which well verifies the theoretical modeling. The deviation at higher frequencies is understandable since the Euler-Bernoulli beam assumption does not cover the shear effect which becomes prominent when operating wavelength becomes comparable to the beam thickness. Aside from the flexural mode, we also observe a longitudinal mode with a much greater group velocity. Since the electrical mode interacts with the flexural mode through the symmetric bending of PZT patches, its coupling with longitudinal modes is in general forbidden. For the interpretation of the mode coupling, we select six representative modes around the intersection and plot their mode shapes in Fig. 2b. Several observations can be made. First, the mechanical and electrical degrees of freedom of the lower branch are in phase, while those of the upper branch are out of phase. Second, in the vicinity of the coupling frequency, modes are hybrid with comparable mechanical and electrical strengths. By contrast, modes are either mechanically or electrically dominant depending on the frequency, owing to the vanishing coupling strength outside the coupling region. Last, at the mechanically dominant modes, such as A2 and C1, the electric field in the PZT patch is not uniform along the thickness, since the nonzero electric response is generated solely by the bending deformation of the host beam. The other four modes exhibit uniform electric field, indicating the existence of electrical propagating modes in the circuit network.

2.4 Transmission characteristics of the hybrid phononic crystal

To examine the performance of the mode veering caused by the mode coupling, we numerically and experimentally investigate the transmittance of a finite HPhC with a uniform circuit network. The geometric and material properties of the host beam and the PZT patches are exactly the same as those given in Fig. 1. We first study on the size effect of the HPhC. As shown in Fig. 3a, two scenarios including 10 and 30 unit cells in the finite HPhC are considered when L=0.3 H. Straight observation indicates that a broad forbidden band featuring multiple transmittance dips appears around the mode veering. Alternatively, the frequencies of the transmittance dips can be theoretically determined by solving $|\mathbf{T}_{\text{total}}(\omega)| = |\mathbf{T}^N(\omega)| = 0$ where N denotes the number of unit cells. This is due to the fact that at transmittance dips we ideally have

$$\mathbf{X}_{\text{out}} = \mathbf{T}_{\text{total}}(\omega)\mathbf{X}_{\text{in}} = \mathbf{0},\tag{27}$$

where $\mathbf{X}_{in} = (\mathbf{Y}_{incidence}, 0, 0)^T$ denotes the incidence, and \mathbf{X}_{out} represents the transmission through the finite HPhC. Another observation is that more unit cells lead to more transmittance

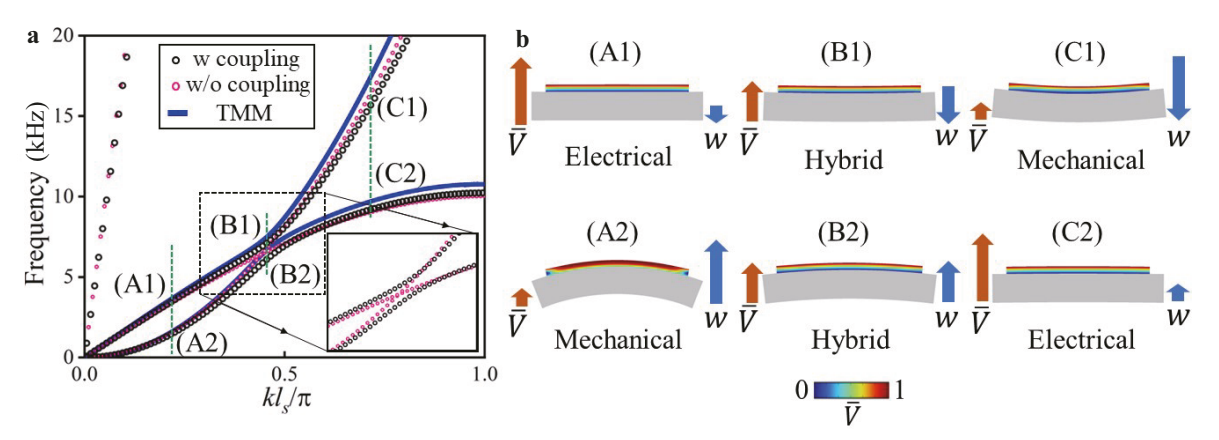


Figure 2 a Dispersion diagram of the HPhC with uniform circuit network and L = 0.3 H. Black and red circles correspond to the numerical simulations with $(\alpha \neq 0)$ and without $(\alpha = 0)$ the effect coupling between electrical and mechanical modes. Blue represents the analytically derived dispersion diagram using Eq. (18) in the presence of the mode coupling. Six representative modes are highlighted. The inset highlights the difference between the cases with and without the coupling. b Mode shapes of the selected six modes in a. The arrow size indicates qualitatively the relative strength of each degree of freedom. The color map represents the normalized electric potential in the PZT patch.

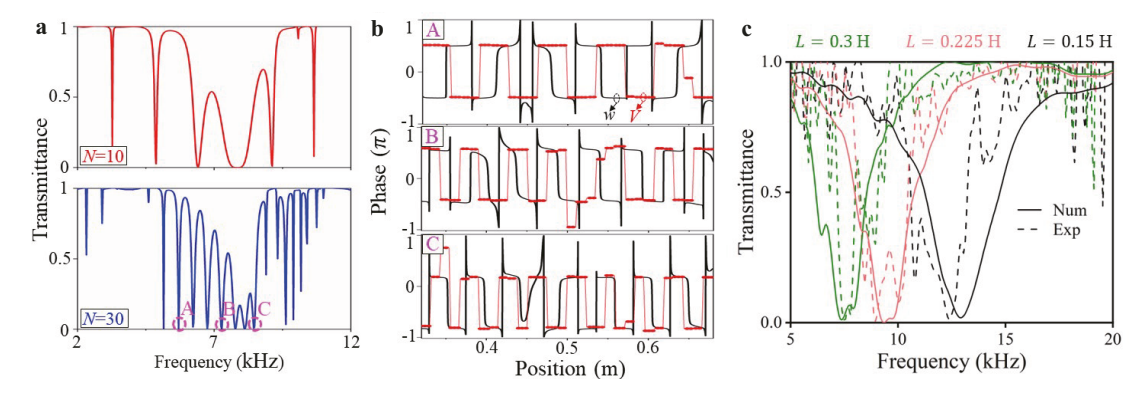


Figure 3 a Numerical transmittance for finite HPhCs including 10 and 30 unit cells when L = 0.3 H. Three representative transmittance dips are highlighted in the case of 30 unit cells. **b** Plots of the phases Arg(w) (black) and Arg(V) (red) at the three highlighted frequencies. **c** Experimentally measured transmittance for a HPhC including 17 unit cells with various L.

dips. It can be understood that the transmittance dips are caused by the global resonances of the finite HPhC. A longer lattice supports more global resonances. Note that the forbidden band behavior due to the mode coupling is unaltered. To interpret the resonances, without loss of generality, we take the case of 30 unit cells as an example and plot the phase distributions for w and V at three representative frequencies in Fig. 3b. Two evident observations can be made. First, the resonance away from the coupling point (mode A in Fig. 3a) is dominated by the out-of-phase hybrid mode (mode B1 in Fig. 2b), while for the resonance at the center of the coupling region (mode B in Fig. 3a), the in-phase and out-of-phase components, corresponding to the modes B2 and B1 in Fig. 2b are mixed with comparable strengths. As for the mode C in Fig. 3a, the in-phase component dominates. Second, bandwidths of dips are controlled by the coupling strength. Specifically, resonances with mixed mode components exhibit wider dips. This is due to the mode coupling at which energy exchange occurs intensively between mechanical and

electrical modes.

To demonstrate the broadband flexural wave mitigation by the HPhC, we conduct experimental measurement for circuit networks with various inductance, say L = 0.15, 0.225,and 0.3 H. The PZT patches are bonded onto the host beam through conductive epoxy. A function generator (Tektronix AFG3022C dual channel arbitrary function generator) is used to generate a 2-cycle broadband tone-burst signal which is later amplified by a power amplifier (KROHN-HITE 7602M wideband amplifier). To excite the flexural incidence from the left, the amplified signal is then applied to a PZT actuator 0.11 m away from the first unit cell of the HPhC. A 3D laser vibrometer (Polytec PSV-400) is used to measure the transient out-of-plane motion on the right side of the HPhC. The collected time-dependent data are then converted in the frequency domain by Fourier transform. As shown in Fig. 3c, broad band gaps are evidently observed for both three cases. Satisfactory agreement can be seen between the simulation and experimental results. In addition, greater inductance

leads to wave mitigation at lower frequencies with narrower bandwidth, since the resonances all shift in accordance with the electrical resonance frequency $f_{\rm res} \propto (C_{\rm p}L)^{-1/2}$. Note that in the simulations, we add a resistor of $R=350~\Omega$ between adjacent nodes in each unit cell, in order to cover the existence of some parasitic resistance carried with the tunable synthetic inductors in experiments. As a result, the transmittance dips are of much smaller quality factors than the numerical ones shown in Fig. 3a. Nevertheless, the experimental demonstration still provides straightforward evidence for the broadband wave mitigation functionality supported by the HPhCs.

3. Dynamic phononic crystals with spatially and temporally modulated circuit networks

The aforementioned HPhCs with uniform circuit networks give rise to only one forbidden band centered at the coupling frequency or band intersection. To further improve the broadband performance, for instance multi-band mitigation, single band intersection is insufficient. In what follows, we investigate the dynamical wave behavior of DPhCs with both spatially and temporally modulated circuit networks, as schematically shown in Fig. 4. The advantage of introducing circuit modulation instead of the mechanical counterpart is two-fold. First, circuit modulation is readily achievable with our programmable synthetic inductors and requires minimal inclusions and modifications of the mechanical beam, which benefits for bettering tunability and reconfigurability while maintaining structural integrity. Second, interactions

of electrical and mechanical modes of different orders are activated. The coupled modes around those intersections appear and are the linear superposition of mechanical and electrical eigenmodes with different intensity coefficients, which can be analytically determined using perturbation methods [30,35]. Based on the above considerations, multi-band wave mitigation is possible and could be more favorable for future applications.

3.1 Dispersion curves for spatial modulation of circuit network

Figure 5a illustrates schematically a DPhC with the spatial modulation $(L_1 \neq L_2)$ of circuit network. To be more specific, the network features alternating inductors, which doubles the lattice constant and makes the DPhC a diatomic system. Other material and geometric properties remain unaltered with respect to the settings given in Fig. 1. The inequity in inductance leads to a Bragg-based band gap for electrical modes. As shown in Fig. 5b, when the coupling is switched off, two intersections can be seen. when the coupling is turned on, the intersection occurs at lower frequency turns into a mode veering between the fundamental flexural band and the acoustical band of electrical mode. This is similar to what we have mentioned in the last section. Interestingly, the fundamental flexural band with positive group velocity also interacts with the optical band of electrical mode with negative group velocity, forming a mode locking around 6.5 kHz [30]. As a result, another Bragg band gap manifests in addition to the veering-induced one discussed previously. To interpret the mode coupling, we plot the mode shapes at

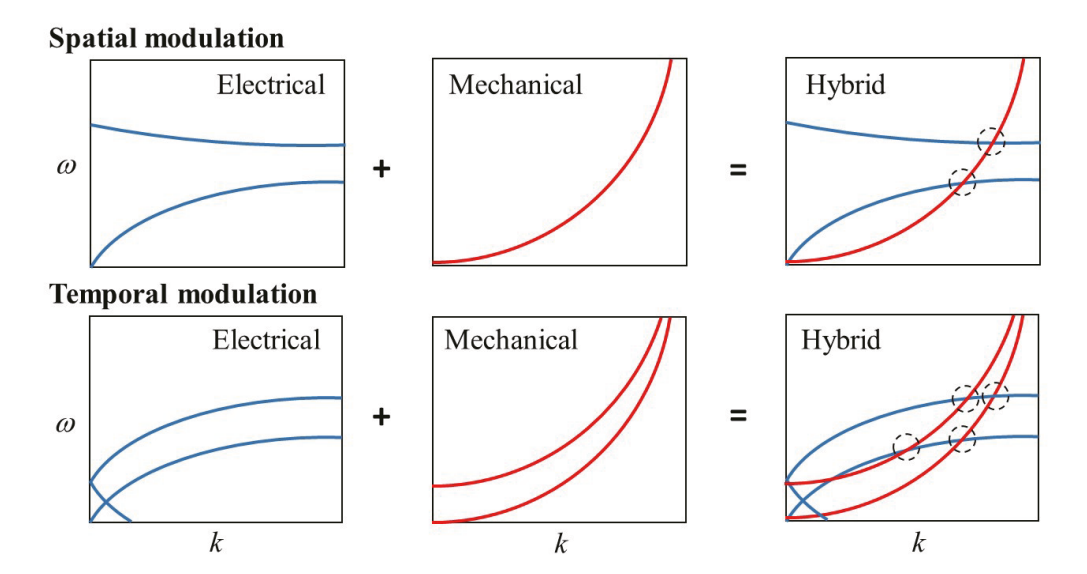


Figure 4 Schematic illustration of the spatial and temporal modulations of circuit network, which can generate more intersections between mechanical and electrical modes (dashed circles) where the phase matching condition is satisfied.

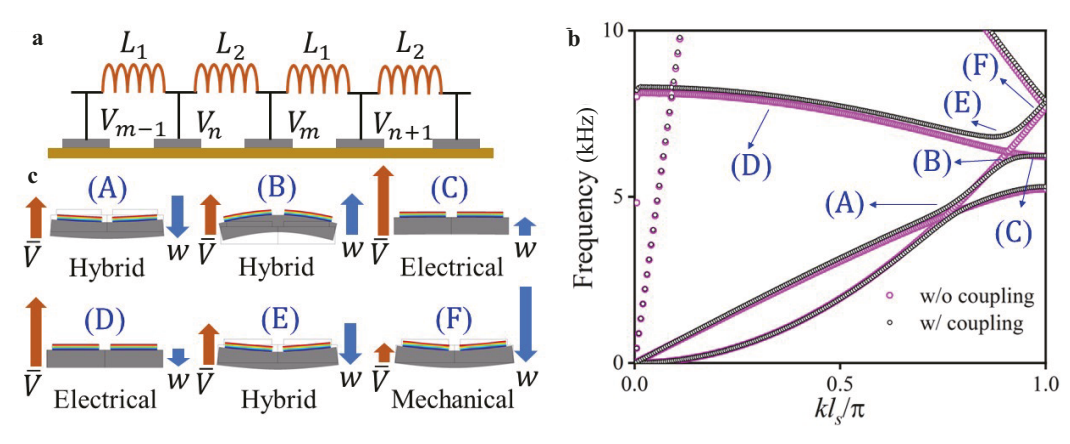


Figure 5 a Schematic of the DPhC with a spatially modulated circuit network. **b** Numerically obtained dispersion curves with and without effective mode coupling when $L_1 = 0.39$ H and $L_2 = 0.55$ H. Other parameters remain unchanged as in the last section. Six representative modes are highlighted. **c** Mode shapes of the highlighted modes.

some representative frequencies in Fig. 5c. As can be seen, around the mode veering and locking, the higher-frequency hybrid modes always exhibit out-of-phase V and w, while the lower-frequency ones have in-phase V and w. Away from the coupling points, modes are either mechanically or electrically dominant.

3.2 Transmission characteristics for spatial modulation of circuit network

Numerical simulation is conducted for a finite HPhC including a spatially modulated circuit network and 17 unit cells. Figure 6a presents the transmittance spectrum possessing multiple dips. The attenuation now occurs within a wider frequency range, compared to the uniform HPhC cases (Fig. 3). Again, we examine the phase distribution of the mechanical and electrical modes in Fig. 6b. It is seen that the resonance modes with narrower bandwidths are dominated by either out-of-phase (mode A) or in-phase (mode D) components. While resonance modes around the coupling regions, i.e., modes B and C, feature hybrid mode components and exhibit lower quality factors due to the intensive energy exchange between electrical and mechanical modes, In the experimental demonstration, the only difference of the current system from the previous one is the inequity in the values of adjacent inductors $L_1 \neq L_2$. Following the same measurement protocol, we observe good agreement between the experiment and simulation in Fig. 6c. To account for the experimental parasitic resistance of tunable synthetic inductors, a resistor of 350 Ω is introduced into each unit cell in the harmonic simulation. As expected, the spatial modulation of circuit network effectively broadens the applicable frequency range for wave mitigation, owing to the occurrence of the additional mode locking compared to the uniform case.

3.3 Dispersion curves for temporal modulation of circuit network

Selective mitigation bands can be achieved by the temporal modulation of circuit network, as it causes linear translations of dispersion curves in the frequency axis. Schematically illustrated in Fig. 7a, the circuit network now consists of identical time-dependent inductors whose inductance is in the form of a cosine function, i.e., $L(t) = L_0 + L_m \cos(\omega_m t)$, where L_m is the modulation magnitude and ω_m is the modulation frequency. To obtain the dispersion curves for such system, we first expand the harmonic solutions for both mechanical and electrical modes, under harmonic modulation, in the forms

$$\mathbf{u} = \sum_{q = -\infty}^{+\infty} \mathbf{u}_q e^{\mathbf{j}(\omega + q\omega_{\mathrm{m}})t},\tag{28}$$

$$V = \sum_{q = -\infty}^{+\infty} V_q e^{j(\omega + q\omega_m)t},$$
(29)

where $\mathbf{u} = (u, v, w)^{\mathrm{T}}$ includes both longitudinal and flexural displacements. In the eigenfrequency analysis, the beam section of the DPhC with temporal modulation is modeled as an isotropic elastic body by the use of the Navier-Lame equation

$$-(\lambda + \mu)\nabla(\nabla \cdot \mathbf{u}) - \mu\nabla^2\mathbf{u} + \rho_s\ddot{\mathbf{u}} = \mathbf{F},\tag{30}$$

where λ and μ are the Lame constants, and \mathbf{F} is an effective body force. Following Eq. (30), the generic *q*th-order governing equation for the beam domain reads

$$-(\lambda + \mu)\nabla(\nabla \cdot \mathbf{u}_a) - \mu\nabla^2\mathbf{u}_a - \rho_s(\omega + q\omega_m)^2\mathbf{u}_a = 0.$$
 (31)

On the other hand, the generic qth-order governing equation for the modulated circuit network is obtained, based on the Fourier expansion and Kirchhoff's current law, as

$$2V_q(\cos kl_s - 1) - (\omega + q\omega_{\rm m})^2 L_0 w_{\rm p} l_{\rm p} \langle D_3^{(q)} \rangle$$

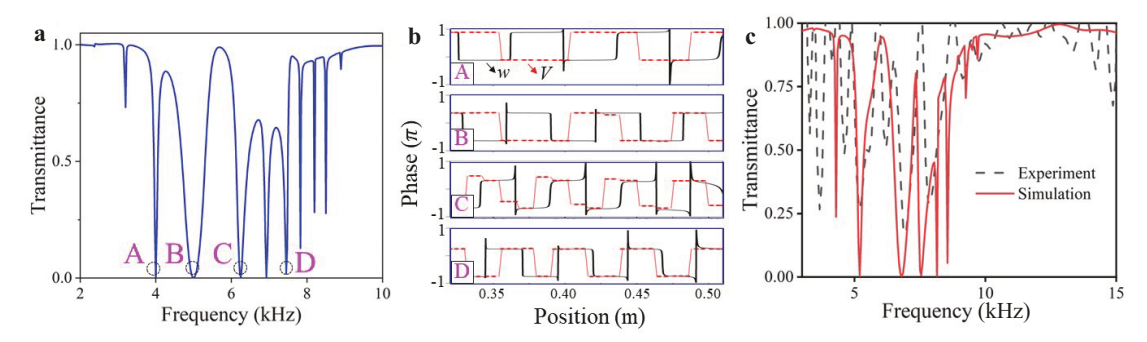


Figure 6 a Numerically obtained transmittance for a finite DPhC with spatially modulated circuit network ($L_1 = 0.39$ H and $L_2 = 0.55$ H) and 17 unit cells. Four transmittance dips are highlighted. **b** Plots of the phases Arg(w) (black) and Arg(V) (red) at the four highlighted frequencies. **c** comparison between experimentally measured transmittance and numerical prediction for the DPhC shown in **a**. In the simulation, a resistor of 350 Ω is connected in series to the circuit component of each unit cell to accommodate the experimental parasitic resistance.

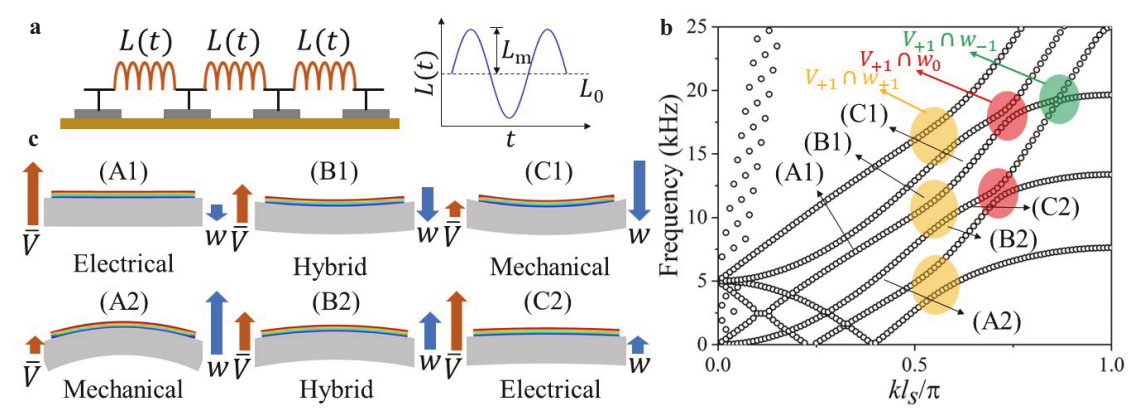


Figure 7 a Schematic of the DPhC with a temporally modulated circuit network. **b** Numerically obtained dispersion curves based on Eqs. (31) and (32) in the consideration of only first-order harmonics when $L_0 = 0.225$ H and $L_{\rm m} = 0.1125$ H. The mechanical part remains unchanged. Three types of mode veerings are indicated, and the representative couplings are labeled, that is $V_{+1} \cap w_{+1}$ (yellow), $V_{+1} \cap w_0$ (red), and $V_{+1} \cap w_{-1}$ (green). Six representative modes for the fundamental harmonics are highlighted. **c** Mode shapes of the highlighted modes.

$$-\sum_{s\neq p}(\omega+s\omega_{\rm m})^2\frac{L_{\rm m}}{2}w_{\rm p}l_{\rm p}\langle D_3^{(s)}\rangle=0, \tag{32}$$

where $\langle \cdot \rangle$ denotes averaging over the top surface of PZT patches, and $w_p l_p \langle D_3^{(q)} \rangle = Q_{(q)}$ is the charge of qth-order generated on the PZT patch. Without loss of generality, here we only consider the interactions between fundamental (q=0) and first-order harmonics $(q=\pm 1)$ for brevity. As a result, Eq. (32) can be recast in a matrix form

$$2(\cos k l_{\rm s} - 1) \begin{bmatrix} V_{-1} \\ V_{0} \\ V_{+1} \end{bmatrix} = \mathbf{Q} \begin{bmatrix} L_{\rm m}/2 \\ L_{0} \\ L_{\rm m}/2 \end{bmatrix}, \tag{33}$$

where

$$\mathbf{Q} = \begin{bmatrix} \omega^2 Q_0 & (\omega - \omega_{\rm m})^2 Q_{-1} & 0\\ (\omega + \omega_{\rm m})^2 Q_{+1} & \omega^2 Q_0 & (\omega - \omega_{\rm m})^2 Q_{-1}\\ 0 & (\omega + \omega_{\rm m})^2 Q_{+1} & \omega^2 Q_0 \end{bmatrix}.$$
(34)

The calculated dispersion curves for $L_0=0.225$ H, $L_{\rm m}=L_0/2=0.1125$ H, and $\omega_{\rm m}=2\pi\times5$ kHz are shown in

Fig. 7b. Straightforwardly observed is that the fundamental branches translate and duplicate linearly by $\omega_{\rm m}$ in the frequency direction thanks to the harmonic modulation of the circuit network. Also multiple mode veerings are induced by the interactions among the considered harmonics. They also perform linear translation of $\omega_{\rm m}$ when more harmonics are taken into account. Specifically, the veerings between identical orders, i.e., $V_a \cap w_a$, highlighted in yellow in Fig. 7b, show the strongest coupling strengths and therefore should be capable of delivering efficient wave mitigation performance. While the veerings formed by different orders, i.e., $V_a \cap w_s$, $q \neq s$, exhibit much weaker coupling strengths as highlighted in Fig. 7b. The interpretation of the mode veering can be done in the same fashion as previously mentioned. We plot the mode shapes mainly for the fundamental branches and find the similar conclusions: away from the coupling point, the modes are either mechanically or electrically dominated, whereas in the vicinity of the coupling the modes are hybrid and display in-phase and out-of-phase field profiles at lower and higher frequencies; also see Fig. 7c.

3.4 Transmission characteristics for temporal modulation of circuit network

The expectation of the temporal modulation, as has been pointed out by Fig. 4, is to form multiple Bragg band gaps. To demonstrate this, 17 unit cells shown in Fig. 7a are used to construct a finite DPhC with the same modulation parameters. Numerical simulation is carried out based on Eqs. (31) and (33). As can be seen from the transmittance spectrum shown in Fig. 8a, two separate band gaps mainly contributed by $V_0 \cap w_0$ and $V_{+1} \cap w_{+1}$ exist showing broadband characteristics. Since the strengths of the veerings $V_q \cap w_s$, $q \neq s$ are underwhelming, their influence on the transmission spectrum is rather minor. The mode shape analysis is performed in Fig. 8b for the selected four resonance dips in Fig. 8a. The four resonances are all hybrid modes with in-phase and out-of-phase components.

One of the key contribution of this work is the experimental evidence of broadband wave isolation characteristics by the temporal modulation. To achieve time-dependent inductance within each unit cell, we program with the external micro-controller (Arduino Mega 2560) linked to a computer to generate a time-varying resistance $R_{\rm dp}(t)$ varying at $\omega_{\rm m}$ in cosine function of time; see Fig. 1c. This effectively realizes the time-varying inductance $L(t) = L_0 + L_m \cos \omega_m t$ illustrated in Fig. 7a. Note that the magnitude of $L_{\rm m}$ should not be close to that of L_0 in order to suppress potential circuit instability. Figure 8c shows the comparison between the experiment and simulation, and satisfactory agreement is observed, verifying the prediction for the temporal modulation. Careful observation finds that the experimental dips are of smaller quality factors, due to the fact that the distribution of parasitic resistance cannot be properly estimated and accommodated in the numerical simulation. In addition, the evident experimental deviations from simulation away from the band gaps are due to the mode veering of higher-order harmonics (second-order, etc), which are not covered by the numerical analysis. Despite these minor discrepancies, the formation of separate forbidden bands are still well distinguishable in the vicinity of the predicted mode veerings. Given that the exotic behavior relies solely on the modulation of the resistor $R_{\rm dp}$, we believe this controllable modulation can be practically deployed in situations where selective multi-band wave mitigation is desired.

3.5 Higher-order temporal modulation of circuit network

It is even possible to achieve higher-order temporal modulation in the DPhC system. To clarify, we add an addition modulation component which makes $L(t) = L_0 + L_{\rm m1} \cos(\omega_{\rm m} t) + L_{\rm m2} \cos(2\omega_{\rm m} t)$. Accordingly, the harmonic governing equations for the electrical parts given in Eq. (32) becomes

$$2V_{p}(\cos k l_{s} - 1) - (\omega + q\omega_{m})^{2} L_{0} w_{p} l_{p} \langle D_{3}^{(q)} \rangle$$

$$= \sum_{s \neq q} (\omega + s\omega_{m})^{2} \frac{L_{m1}}{2} w_{p} l_{p} \langle D_{3}^{(s)} \rangle$$

$$+ \sum_{s \neq q} (\omega + 2s\omega_{m})^{2} \frac{L_{m2}}{2} w_{p} l_{p} \langle D_{3}^{(2s)} \rangle. \tag{35}$$

Figure 9a provides the dispersion diagram of the higher-order temporal modulation, numerically retrieved based on Eq. (35). For brevity, we again have considered only fundamental (q=0) and first-order harmonics $(q=\pm 1)$ and their interactions. As can be seen, the fundamental branches are translated linearly by $\pm \omega_{\rm m}$ due to the first-order modulation and by $\pm 2\omega_{\rm m}$ due to the additional second-order modulation. As a result, five branches can be seen for the higher-order modulation (red in Fig. 9a) unlike the singly modulated case (blue in Fig. 9a) discussed in the previous section. Evidently, multiple mode veerings appear. Among them, $V_q \cap w_q$ possesses the greatest coupling strength and hence should be capable of delivering broadband wave mitigation for flexural waves. Indeed, the transmittance spectra presented in Fig.

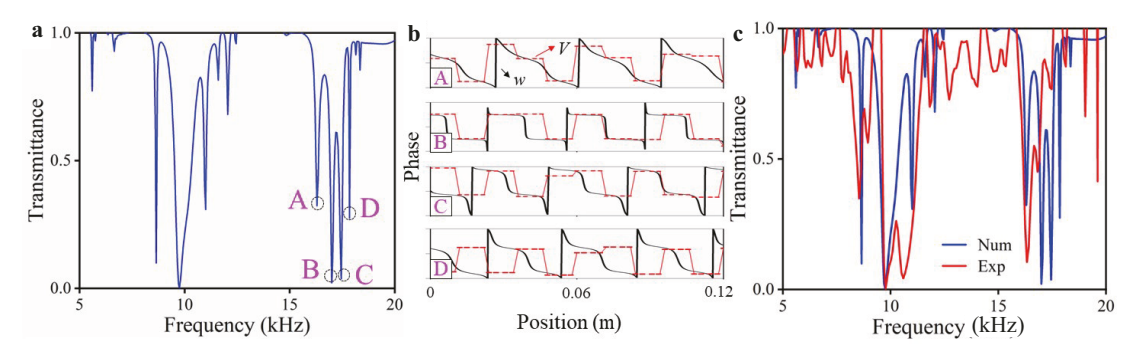


Figure 8 a Numerically obtained transmittance for a finite DPhC including temporally modulated circuit network ($L_0 = 0.225$ H and $L_m = 0.1125$ H) and 17 unit cells. Four transmittance dips are highlighted. **b** Plots of the phases Arg(w) (black) and Arg(V) (red) at the four highlighted resonance modes. **c** Experimentally measured transmittance (red) for the HPhC with temporal modulation and its comparison with the corresponding numerical simulation (blue).

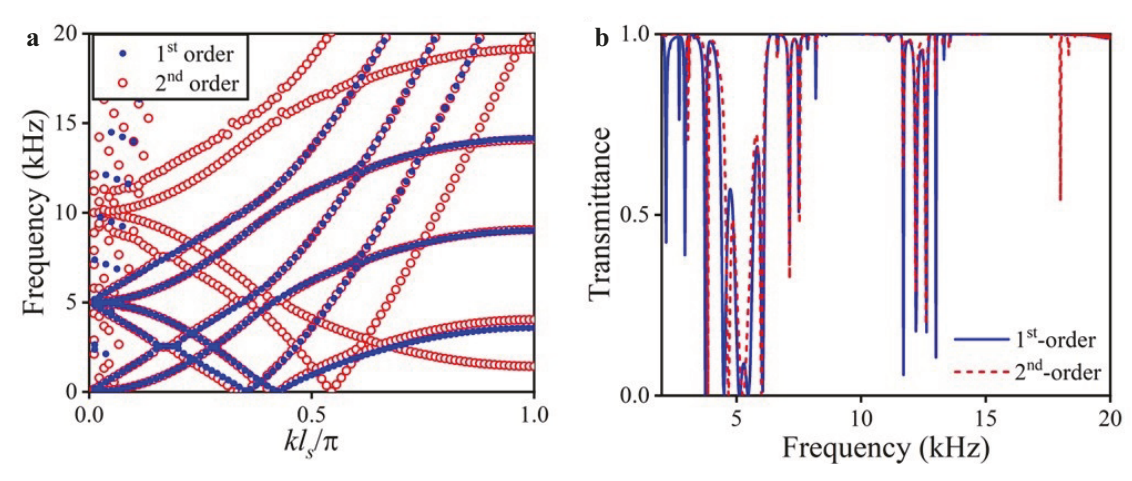


Figure 9 a Comparison between dispersion curves for first- and second-order temporal modulation, with the first-order modulation (blue) being $L(t) = L_0 + L_{\rm m1} \cos(\omega_{\rm m}t)$ and the second-order one (red) $L(t) = L_0 + L_{\rm m1} \cos(\omega_{\rm m}t) + L_{\rm m2} \cos(2\omega_{\rm m}t)$. Here, $L_0 = 0.5$ H, $L_{\rm m1} = 0.25$ H, $L_{\rm m2} = 0.15$ H, and $\omega_{\rm m} = 2\pi \times 5$ kHz are selected for clear demonstration. **b** Numerically obtained transmittance spectra for both first- and second-order temporal modulation. Both the finite DPhCs with various temporal modulation include 17 unit cells.

9b confirms this behavior. As one can see, three band gaps are formed in the case of higher-order modulation within the frequency range of interest (red in Fig. 9b). On the contrary, only two band gaps are seen for the first-order modulation (blue in Fig. 9b). The additional band gap for the higher-order modulation is due to the introduction of $L_{\rm m2}\cos 2\omega_{\rm m}t$. Note that the inclusion of higher-order harmonics will introduce more transmittance dips between the major veerings $V_q \cap w_q$.

4. Conclusion

In this work, We first revisit the concept of the onedimensional hybrid phononic crystal with uniform circuit networks. To improve the wave mitigation functionality, we then provide both theoretical and experimental investigation of the dynamic phononic crystal integrated with spatially and temporally modulated circuit networks. The considered modulation gives rise to addition interactions between mechanical and electrical modes within the frequency range of interest. This effectively extents the interaction regions and broadens the applicable frequency range for flexural wave mitigation. In addition, the realization of both modulations is based on the convenient tuning of a circuit component, which is favorable for practical applications. Given the completeness of this study, we believe the dynamical phononic crystal can pave the way for the next-generation applications such as tunable multi-band filters.

Author contributions Guoliang Huang and Yangyang Chen designed the research. Qian Wu, Yangyang Chen and Honghua Qian carried out the numerical simulation, set up the experiment set-up and processed the experimental data. Guoliang Huang supervised the research. Acknowledgements This work was supported by the Air Force Office of Scientific Research (Grant No. 9550-20-1-0279) with Program Manager Dr. Byung-Lip (Les) Lee and NSF CMMI, USA (Grant No. 1930873).

- 1 J. J. Hollkamp, Multimodal passive vibration suppression with piezoelectric materials and resonant shunts, J. Intell. Mater. Syst. Struct. 5, 49 (1994).
- 2 B. S. Beck, K. A. Cunefare, M. Ruzzene, and M. Collet, Experimental analysis of a cantilever beam with a shunted piezoelectric periodic array, J. Intell. Mater. Syst. Struct. 22, 1177 (2011).
- 3 A. Spadoni, M. Ruzzene, and K. Cunefare, Vibration and wave propagation control of plates with periodic arrays of shunted piezoelectric patches, J. Intell. Mater. Syst. Struct. 20, 979 (2009).
- 4 L. Brillouin, Wave Propagation in Periodic Structures: Electric Filters and Crystal Lattices, 2nd ed. (McGraw-Hill Book Company, Dover, 1946).
- 5 X. Zhou, and G. Hu, Analytic model of elastic metamaterials with local resonances, Phys. Rev. B 79, 195109 (2009).
- 6 G. Ma, and P. Sheng, Acoustic metamaterials: From local resonances to broad horizons, Sci. Adv. 2, e1501595 (2016).
- 7 Z. Liu, X. Zhang, Y. Mao, Y. Y. Zhu, Z. Yang, C. T. Chan, and P. Sheng, Locally resonant sonic materials, Science 289, 1734 (2000).
- M. Nouh, O. Aldraihem, and A. Baz, Wave propagation in metamaterial plates with periodic local resonances, J. Sound Vib. 341, 53 (2015).
- 9 Y. Lai, Y. Wu, P. Sheng, and Z. Q. Zhang, Hybrid elastic solids, Nat. Mater 10, 620 (2011).
- 10 V. Laude, Phononic Crystals: Artificial Crystals for Sonic, Acoustic, and Elastic Waves (Walter de Gruyter GmbH & Co KG, Berlin, 2015).
- 11 H. Zhao, Y. Liu, G. Wang, J. Wen, D. Yu, X. Han, and X. Wen, Resonance modes and gap formation in a two-dimensional solid phononic crystal, Phys. Rev. B 72, 012301 (2005).
- Y. Jin, N. Fernez, Y. Pennec, B. Bonello, R. P. Moiseyenko, S. Hémon, Y. Pan, and B. Djafari-Rouhani, Tunable waveguide and cavity in a phononic crystal plate by controlling whispering-gallery modes in hollow pillars, Phys. Rev. B 93, 054109 (2016).
- 13 D. Yu, J. Wen, H. Zhao, Y. Liu, and X. Wen, Vibration reduction by using the idea of phononic crystals in a pipe-conveying fluid, J. Sound Vib. 318, 193 (2008).
- 14 M. H. Lu, L. Feng, and Y. F. Chen, Phononic crystals and acoustic metamaterials, Mater. Today 12, 34 (2009).
- 15 C. P. Wei, and C. X. Xue, Bending waves of a rectangular piezoelectric

- laminated beam, Acta Mech. Sin. 36, 1099 (2020).
- 16 G. Wang, S. Chen, and J. Wen, Low-frequency locally resonant band gaps induced by arrays of resonant shunts with Antoniou's circuit: Experimental investigation on beams, Smart Mater. Struct. 20, 015026 (2010)
- 17 J. A. B. Gripp, and D. A. Rade, Vibration and noise control using shunted piezoelectric transducers: A review, Mech. Syst. Signal Process. 112, 359 (2018).
- 18 Y. Wang, C. Zhang, W. Chen, Z. Li, M. V. Golub, and S. I. Fomenko, Precise and target-oriented control of the low-frequency Lamb wave bandgaps, J. Sound Vib. 511, 116367 (2021).
- 19 B. Hu, J. Liu, Y. Wang, B. Zhang, and H. Shen, Wave propagation in graphene reinforced piezoelectric sandwich nanoplates via high-order nonlocal strain gradient theory, Acta Mech. Sin. 37, 1446 (2021).
- Y. Wang, Z. Li, W. Chen, C. Zhang, and J. Zhu, Free vibration and active control of pre-stretched multilayered electroactive plates, Int. J. Solids Struct. 180-181, 108 (2019).
- 21 Z. Y. Li, Y. Z. Wang, T. X. Ma, Y. F. Zheng, C. Zhang, and F. M. Li, A self-sensing and self-actuating metamaterial sandwich structure for the low-frequency vibration mitigation and isolation, Compos. Struct. 297, 115894 (2022).
- 22 R. Xia, J. Yi, Z. Chen, and Z. Li, *In situ* steering of shear horizontal waves in a plate by a tunable electromechanical resonant elastic metasurface, J. Phys. D-Appl. Phys. 53, 095302 (2019).
- 23 Q. Wu, X. Zhang, P. Shivashankar, Y. Chen, and G. Huang, Independent flexural wave frequency conversion by a linear active metalayer, Phys. Rev. Lett. 128, 244301 (2022).
- 24 R. Xia, S. Shao, J. Yi, K. Zheng, M. Negahban, and Z. Li, Tunable asymmetric transmission of Lamb waves in piezoelectric bimorph plates by electric boundary design, Compos. Struct. 300, 116111 (2022)
- 25 Q. Wu, Y. Chen, and G. Huang, Asymmetric scattering of flexural waves in a parity-time symmetric metamaterial beam, J. Acoust. Soc. Am. 146, 850 (2019).
- 26 D. Braghini, L. G. G. Villani, M. I. N. Rosa, and J. R. de F Arruda, Non-Hermitian elastic waveguides with piezoelectric feedback actuation: Non-reciprocal bands and skin modes, J. Phys. D-Appl. Phys. 54, 285302 (2021), arXiv: 2102.07172.
- 27 C. Maurini, F. dell'Isola, and D. Del Vescovo, Comparison of piezoelectronic networks acting as distributed vibration absorbers, Mech. Syst. Signal Process. 18, 1243 (2004).
- 28 H. Yu, and K. W. Wang, Piezoelectric Networks for vibration suppression of mistuned bladed disks, J. Vib. Acoust. 129, 559 (2007).
- 29 A. E. Bergamini, M. Zündel, E. A. Flores Parra, T. Delpero, M.

- Ruzzene, and P. Ermanni, Hybrid dispersive media with controllable wave propagation: A new take on smart materials, J. Appl. Phys. 118, 154310 (2015).
- 30 B. R. Mace, and E. Manconi, Wave motion and dispersion phenomena: Veering, locking and strong coupling effects, J. Acoust. Soc. Am. 131, 1015 (2012).
- 31 E. A. Flores Parra, A. Bergamini, L. Kamm, P. Zbinden, and P. Ermanni, Implementation of integrated 1D hybrid phononic crystal through miniaturized programmable virtual inductances, Smart Mater. Struct. 26, 067001 (2017).
- 32 E. A. Flores Parra, A. Bergamini, B. Van Damme, and P. Ermanni, Controllable wave propagation of hybrid dispersive media with LC high-pass and band-pass networks, Appl. Phys. Lett. 110, 184103 (2017)
- 33 E. A. Flores Parra, A. Bergamini, B. Lossouarn, B. Van Damme, M. Cenedese, and P. Ermanni, Bandgap control with local and interconnected LC piezoelectric shunts, Appl. Phys. Lett. 111, 111902 (2017).
- 34 Y. Zheng, J. Zhang, Y. Qu, and G. Meng, Adaptive nonreciprocal wave attenuation in linear piezoelectric metastructures shunted with one-way electrical transmission lines, J. Sound Vib. 503, 116113 (2021).
- 35 Q. Wu, H. Chen, H. Nassar, and G. Huang, Non-reciprocal Rayleigh wave propagation in space-time modulated surface, J. Mech. Phys. Solids 146, 104196 (2021).
- 36 X. Xu, Q. Wu, H. Chen, H. Nassar, Y. Chen, A. Norris, M. R. Haberman, and G. Huang, Physical observation of a robust acoustic pumping in waveguides with dynamic boundary, Phys. Rev. Lett. 125, 253901 (2020), arXiv: 2006.07348.
- J. Marconi, E. Riva, M. Di Ronco, G. Cazzulani, F. Braghin, and M. Ruzzene, Experimental observation of nonreciprocal band gaps in a space-time-modulated beam using a shunted piezoelectric array, Phys. Rev. Appl. 13, 031001 (2020), arXiv: 1909.13224.
- 38 G. Trainiti, Y. Xia, J. Marconi, G. Cazzulani, A. Erturk, and M. Ruzzene, Time-periodic stiffness modulation in elastic metamaterials for selective wave filtering: Theory and experiment, Phys. Rev. Lett. 122, 124301 (2019), arXiv: 1804.09209.
- 39 N. W. Hagood, and A. von Flotow, Damping of structural vibrations with piezoelectric materials and passive electrical networks, J. Sound Vib. 146, 243 (1991).
- 40 Q. Wu, P. Shivashankar, X. Xu, Y. Chen, and G. Huang, Engineering nonreciprocal wave dispersion in a nonlocal micropolar metabeam, J. Compos. Mater. 57, 771 (2023).
- 41 Y. Chen, X. Li, C. Scheibner, V. Vitelli, and G. Huang, Realization of active metamaterials with odd micropolar elasticity, Nat. Commun. 12, 5935 (2021), arXiv: 2009.07329.

受时空调制电网控制的动态声子晶体

吴谦,钱泓桦,陈洋洋,黄国良

摘要 宽频弹性波衰减技术在现代工程应用中有不可或缺的地位.本文提出了一种基于时间/空间调制电网和压电材料的动态声子晶体并进行了实验验证.该动态声子晶体可以在多频带上实现对弯曲波传输的衰减,并对衰减频带进行调控.压电分流电路为机械模态和电模态提供了能量交换的同时也产生了布拉格带隙.该动态声子晶体仅需对电网进行时间/空间调制以实现可调制的宽频带弯曲波衰减.其中,通过对电网进行空间调制可实现两条布拉格带隙从而扩大了机电耦合以及弯曲波衰减的频率范围.另一方面,时间调制使机电耦合的模态频率产生线性平移从而生成了多条时间-布拉格带隙.更重要的是,本文提供了一种简易的弯曲波带隙调谐方式,即只对单一电阻进行控制.相关实验也进一步验证了时间/空间调制对弯曲波传输的影响.该动态声子晶体可以为下一代可调谐的多频带滤波器等设备提供新思路.